

Self-organizing pneumatic apertures

Raphael Kay^{a,b,c}, Charlie Katrycz^a, Kevin Nitiema^c, Ethan Heimlich^d, Benjamin D. Hatton^a

^aDepartment of Materials Science and Engineering, University of Toronto

^bDepartment of Mechanical and Industrial Engineering, University of Toronto

^cJohn H. Daniels Faculty of Architecture, Landscape, and Design, University of Toronto

^dDepartment of Statistical Sciences, University of Toronto

Abstract

Building materials that dynamically modulate optical transparency can drastically augment the performance of indoor heating, cooling, and lighting systems, and significantly improve energy efficiency. Existing optoregulatory platforms, however, often rely on costly or sophisticated microelectronic, electrochemical, or nanophotonic mechanisms, severely limiting the length-scale of application functionality. Here, we show that pneumatic pressure can be a simple and scalable approach to tune light penetration through a confined fluidic layer. Air pressure was used to control the morphology and depth of a self-organizing bubble within a viscous pigment fluid, modulating visible light transmission through this ‘aperture’ between 0-80%. Mathematical models are in good agreement with experimental findings, allowing us to predict and program our system’s optical behaviour. Over large areas, digital pneumatic control can facilitate a multiplexed response, enabling inexpensive, simple, and scalable choreographable optical performance.

Introduction

We spend a large proportion of our energy conditioning the indoor environment¹. More than 50% of the electricity consumed in the United States, for instance, is dedicated to heating, cooling, and lighting residential and commercial buildings^{1,2}, while up to 70% of the energy required for indoor agriculture is devoted to providing artificial illumination alone³.

Underpinning these significant loads in buildings is the static design of their outer facade. Fixed windows and walls cannot dynamically regulate incident solar flux, often resulting in undesirable variations in interior illumination and temperature. As a result, we typically rely on internal heating, cooling, and lighting systems to compensate for changes in the solar environment. This leads to large energetic expenditures; in the United States, for example, enviro-regulatory (HVAC) systems consume over 50% of the building energy total, and 20% of the national energy total¹.

As an alternative approach, there is growing momentum to develop dynamic facade materials, capable of regulating solar flux directly at the building surface^{4,5}. Embedded solar control immediately at the interface between indoor and outdoor environments has the potential to alleviate a significant proportion of a building’s internal energetic burden – preconditioning indoor environments using tunable material properties rather than postconditioning indoor environments using air conditioners, heaters, and electric lighting systems⁵⁻⁷.

Despite this promise, typical optically-adaptive materials have struggled to feasibly scale to the length-scale of a building⁵. Structurally-coloured photonic materials with nanoscopic topological features, for instance, often require expensive or macroscopically-unstable self-assembly⁸. Visible-⁹ and infrared-adaptive¹⁰ dielectric materials, on the other hand, have high operating voltages and, along with liquid crystal¹¹⁻¹³ and suspended particle^{14,15} technologies, require a consistent power supply to remain in a

coloured, cloudy, or non-transparent configuration. Electrochromic materials rely on oxidation-reduction reactions and multilayer sputter deposition fabrication procedures^{16,17}, and have high production costs^{16,18-21} and complexity^{16,19,22}. While thermo-^{16,23-29} and photo-chromogenics^{11,16,23,25-27}, as well as hygroscopics³⁰⁻³², are sensitive to environmental stimuli (temperature, light, and moisture, respectively), making distributed control and digital configurability a difficulty. Lastly, mechanically-actuated structures that modulate shading material density, including rotating frits³³, bending elements³⁴, and louvers^{35,36}, are either low-resolution, rigid, or prone to breakage³⁷. Accordingly, the development of large-area materials that can achieve high-resolution photo-switchability without the productional or operational limitations posed by conventional mechanisms represents an important technical challenge.

Within our group, micro- and millifluidic materials have gained particular attention for such a pursuit; we have recently shown that small volumes of confined liquid can be easily manipulated and digitally switched within inexpensive, large-area devices to achieve minute-scale control over light transmission^{6,38-42}. Systems with embedded channel structures enable pre-patterned spatial control of fluid flow^{38,39}, while materials that enclose a two-dimensional cavity for multifluid activity enable more dynamic flow tunability and subsequent patterning effects^{6,40-42}. In this regard, we recently developed a system for reversibly controlling the shape and size of aqueous pigment injections within a more viscous transparent oil layer⁶. Leveraging a common hydrodynamic branching instability (viscous fingering), it was shown that modulating the injection flow rate and volume could vary the pigment's branching morphology and size, impacting total light transmission through the layer. Experiments within similar devices revealed how the global shape of injected pigment droplets could be varied using dynamic flow field configurability⁴⁰.

Despite these achievements in multiscale pattern control and digital tunability, storing and accessing these active liquids has proven to be an operational limitation, with yet-unaddressed mechanical concerns over maintenance, system longevity, and durability.

Here, we show that analogous liquid-less pneumatic systems, which make use of a much more readily-accessible working fluid – the surrounding air – can accomplish equivalent optical switchability. By tuning the injection flow rate, and subsequent gaseous pressure, of an injected air bubble within a confined pigment layer, we achieve spatiotemporal patterning of optical transparency. We develop a recursive mathematical model and leverage accessible digital electronics to predict and tune single cell and multiplexed behaviours. This optofluidic system, taking advantage of a limitless and spatially-continuous supply of surrounding air, represents a mechanically-robust, easily-scalable, and inexpensive chromogenic platform for accomplishing digitally tunable optical modulation and pattern control in large-area materials.

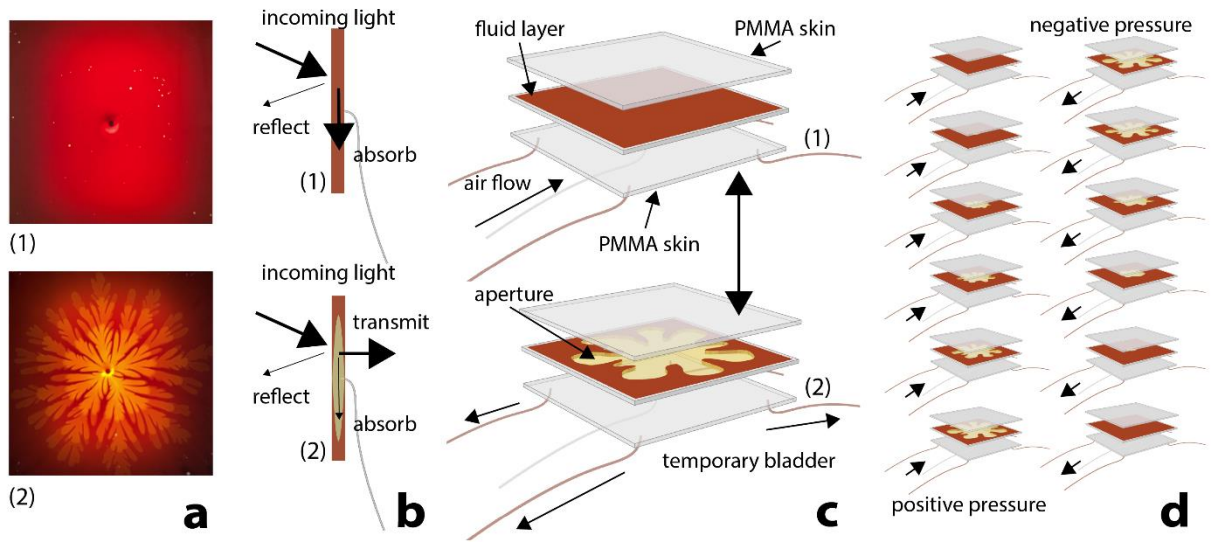


Figure 1. Design and reversible operation of shape-programmable aperture. (a) (1) Stable fluid layer prior to air injection. (2) Superimposed aperture opening sequence with positive air pressure. (b) Schematic showing ability of system to control light transmittance with aperture activation, where (1) represents closed state and (2) represents open state. (c) Design of fluidic device in which aperture is activated. (1) represents closed state and (2) represents open state. (d) From top-left to bottom-right, showing aperture opening and closing sequence, where positive pressure is applied for opening and negative pressure is applied for closing.

Results

We fabricated simple liquid-filled cells within which reversible injections of air – ‘apertures’ – could be spatially programmed (Fig. 1a). A 30x30 cm², 1-mm-thick pigment layer – in this case, molasses, chosen for its high viscosity, low cost, and everyday accessibility – was sandwiched between two rigid, 6-mm-thick, polymethyl methacrylate (PMMA) plates. This configuration, known more formally as a Hele-Shaw (HS) cell, included a central inlet port within one of the PMMA plates for pneumatic injections, as well as four outer ‘bladders’, protruding from the four corners of the cell, to temporarily store the displaced molasses (Fig. 1c). The inlet hose was connected to a digital syringe pump and pressure sensor (Fig. 1e). Air was drawn from the atmosphere, compressed, and, when sufficiently pressurized, expanded into the pigment layer to alter its optical transmissivity (Fig. 1b, d). Oppositely, when the pump flow was reversed, the air bubble became negatively pressurized, collapsing back to its source, and returning the pigment layer to its opaque state.

Tuning aperture morphology with flow rate

When a fluid of low viscosity (e.g., air) displaces a second fluid of higher viscosity (e.g., molasses) between two closely-spaced parallel plates (HS cell), the fluid of low viscosity typically branches as it flows, forming finger-tip-like structures^{43,44}. The critical width of the branching features, set by the most unstable wavelength λ_c , can be controlled by altering the interfacial surface tension σ , injection velocity V , distance between plates b , or difference between host and guest fluid viscosity $\Delta n = n_h - n_g$, using a relation derived by Saffman and Taylor⁴⁵ in equation (1).

$$(1) \quad \lambda_c = \pi b \sqrt{\frac{\sigma}{3V\Delta n}}$$

Experimentally, for a given cell (b) and fluid ($\sigma, \Delta n$) configuration, we can accordingly modulate λ_c by tuning the injection velocity through digital control over an injection flow rate. At higher flow rates, we can expect high interfacial velocities, leading to more amplified branching, given by a larger amplification factor a_λ for a given finger width of instability λ^{45} ,

$$(2) \quad a_\lambda = 3V\Delta n - \sigma \left(\frac{\pi b}{\lambda} \right)^2$$

Equation (2) demonstrates that greater injection velocities should induce greater branching amplification, finer branching features, and more rapid tip-splitting events. For our purposes, we take advantage of how such predictable branching behaviour impacts the overall morphology, and area coverage, of an expanding pneumatic aperture.

Fig. 2a shows five cyclic injection-retraction sequences of a budding and collapsing pneumatic aperture within our molasses-filled HS cell. We experimentally controlled the pneumatic injection flow rate between 0.75-225 mL/min. As expected, higher flow rates led to higher internal pressure increases (Fig. 2b-c), causing much more rapid interfacial growth, amplified branching events, finer and more numerous finger features (Fig. 2d), and, as a result, lower aperture area fractions during expansion within the cell (Fig. 2e). Overall, we demonstrated that by modulating the volume of injected air within the molasses layer between 0-15 mL, aperture area fraction could be tuned up to 55% within a square-shaped panel geometry (Fig. 2e). Additionally, we demonstrated that by modulating the injection flow rate between 0.75-225 mL/min, causing local maximal pneumatic pressure increases between \sim 0-60 kPa, radius-normalized aperture area fraction could be tuned by 20%, between 35-55% (Fig. 2f). Volume-tuning accordingly represents an accessible mechanism to control the *size* of an expanding aperture. Flow-rate-tuning, on the hand, represents an accessible mechanism to control the *shape* of an expanding aperture.

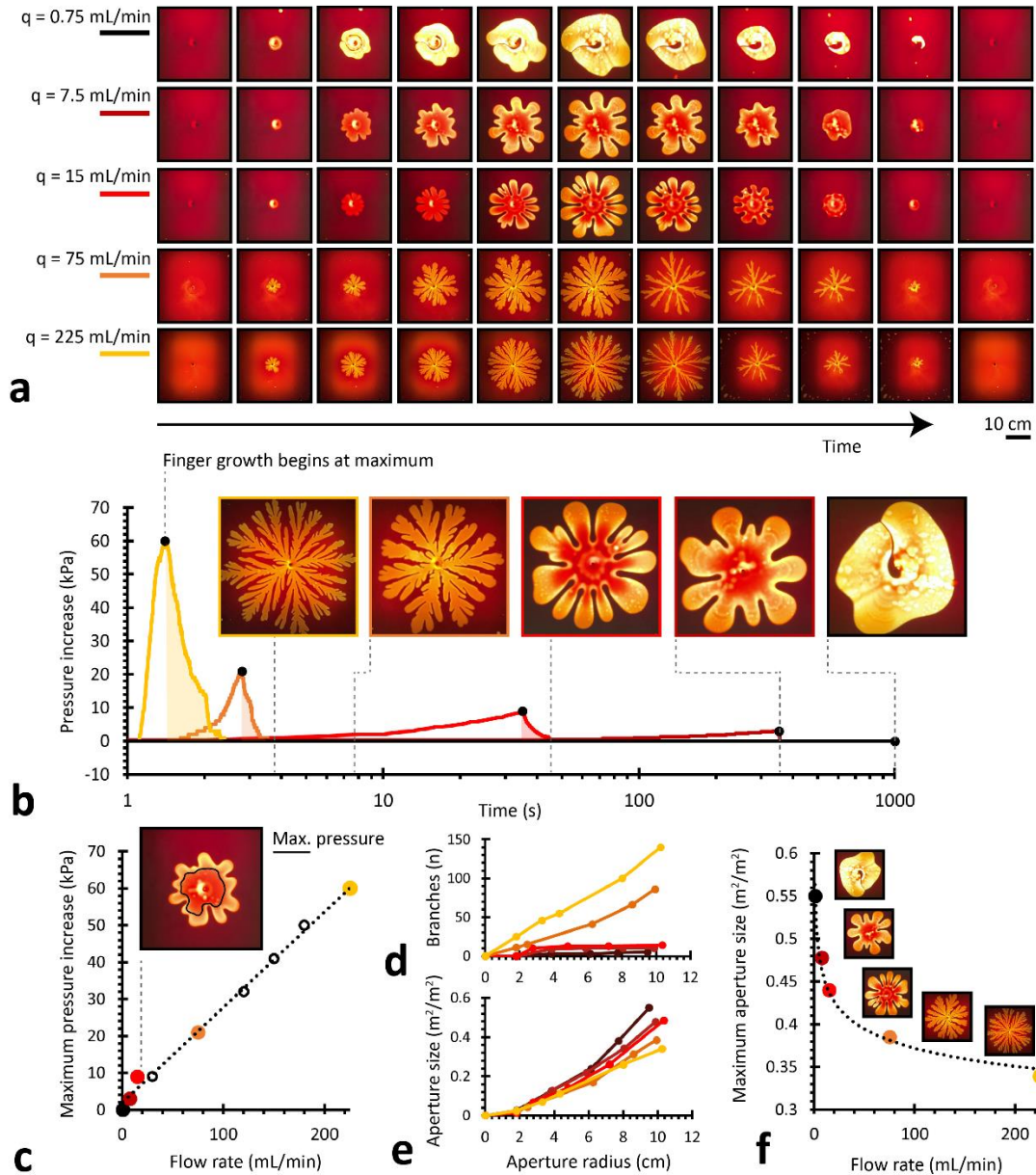


Figure 2. Aperture morphology can be programmed with nominal flow rate. (a) Reversible aperture expansion and retraction sequence at five constant flow rates (0.75-225 mL/min). (b) Air pressure within aperture during expansion sequence. Maximum pressure occurs directly before branching begins, after which air pressure returns to P_{atm} . Images correspond to final morphology for each aperture. (c) Maximum air pressure increases linearly with flow rate. Maximum air pressure occurs at point in growth directly before branching begins, illustrated by black line in photo. (d) Number of branches increases as the apertures grows in radius, but to a greater degree for apertures assembled at higher flow rates. (e) Aperture area increases as the apertures grows in radius, but to a greater degree for apertures assembled at lower flow rates, due to less branched morphologies. (f) The maximum aperture size, within a cell with a fixed radius, can therefore be programmed with flow rate. Higher flow rates produce apertures with more branched morphologies, and less area coverage.

Tuning aperture wetting and opacity with flow rate

When a long fluid bubble expands or travels within a confined liquid-filled geometry (e.g., HS cell or capillary tube), it tends to leave a thin film of non-displaced liquid along the walls of its fluid container (e.g., above and below it within a HS cell)⁴⁶. Bretherton first showed that the thickness of this film h is linearly proportional to the capillary number $Ca = V \cdot \left(\frac{\eta h}{\sigma}\right)$, so long as h is negligible compared to the container gap b , or roughly when $h/b < 0.05$. This relation has since been modified and experimentally verified by Aussillous and Qu  r  ⁴⁷ to generalize film thickness h/b as a function of Ca ,

$$(3) \quad h = \frac{0.5b \cdot \varphi \cdot Ca^{2/3}}{1 + ([\varphi \cdot \omega] \cdot Ca^3)}$$

Fundamentally, equation (3) reveals that as the injection velocity (proportional to Ca) increases, the thickness of the remaining film decreases, where φ and ω represent fitting parameters to describe h within a given geometry (Fig. 3a). The optical consequence of this interaction is critical: we can use injection flow rate to modulate molasses film thickness – or the optical path length of absorbing media through which incident light must travel. Put more simply, we can use injection flow rate to modulate aperture transparency.

Fig. 3b shows five pneumatic aperture structures, generated with flow rates between 0.75-225 mL/min, and constant backlighting from a white LED source (400 lux). We used coloured and grey-scale pixel values from still video frames to approximate temporal light transmission within apertures. As expected, colour darkened, indicating a decrease in transmissivity, for pixels sampled from finger regions within apertures assembled at increasing flow rates (Fig. 3b). Also, as expected, the grey-scale value also darkened, indicating a decrease in transmissivity, for pixels averaged across entire aperture regions at increasing flow rates (Fig. 3b-c).

We validated these results experimentally, calculating transmissivity by dividing the measured incident light (400 lux) by the measured transmitted light behind the cell, and then multiplying this transmission value by the aperture area fraction (Fig. 3d). These transmissivity characterization methods showed good agreement, and, by sampling video frames for small ($\sim 1 \text{ mm}^2$) aperture regions, we quantified how both digitized (black dots) and measured (orange dots) transmissivity varied with local aperture front velocity during injection (Fig. 3e).

This trend was further verified by quantifying the optical density of our light-absorbing molasses fluid. Using spectrophotometry, we measured optical absorbance by experimentally varying h between 100-1000 μm , at $\sim 100 \mu\text{m}$ depth steps (Fig. 3f, orange dots). Using the Beer-Lambert law⁴⁸ – equation (4) – which relates optical absorbance A to an absorption coefficient ε and layer thickness x (or $2h$ within our HS system), we found an absorption coefficient of $\varepsilon = 2700 \text{ m}^{-1}$ for our molasses fluid (Fig. 3f, slope of dotted black line).

$$(4) \quad A = x\varepsilon, \text{ or } A = 2h \cdot \varepsilon$$

Using this established flow-rate-dependent opacity control, we demonstrated more advanced optical patternability. Extended Data Fig. 1 shows how variable pneumatic flows can ‘deposit’ molasses rings with variable thickness and optical transparency. Such digital accessibility enables radially-tunable optical control, with good long-term (hour-scale) structural stability.

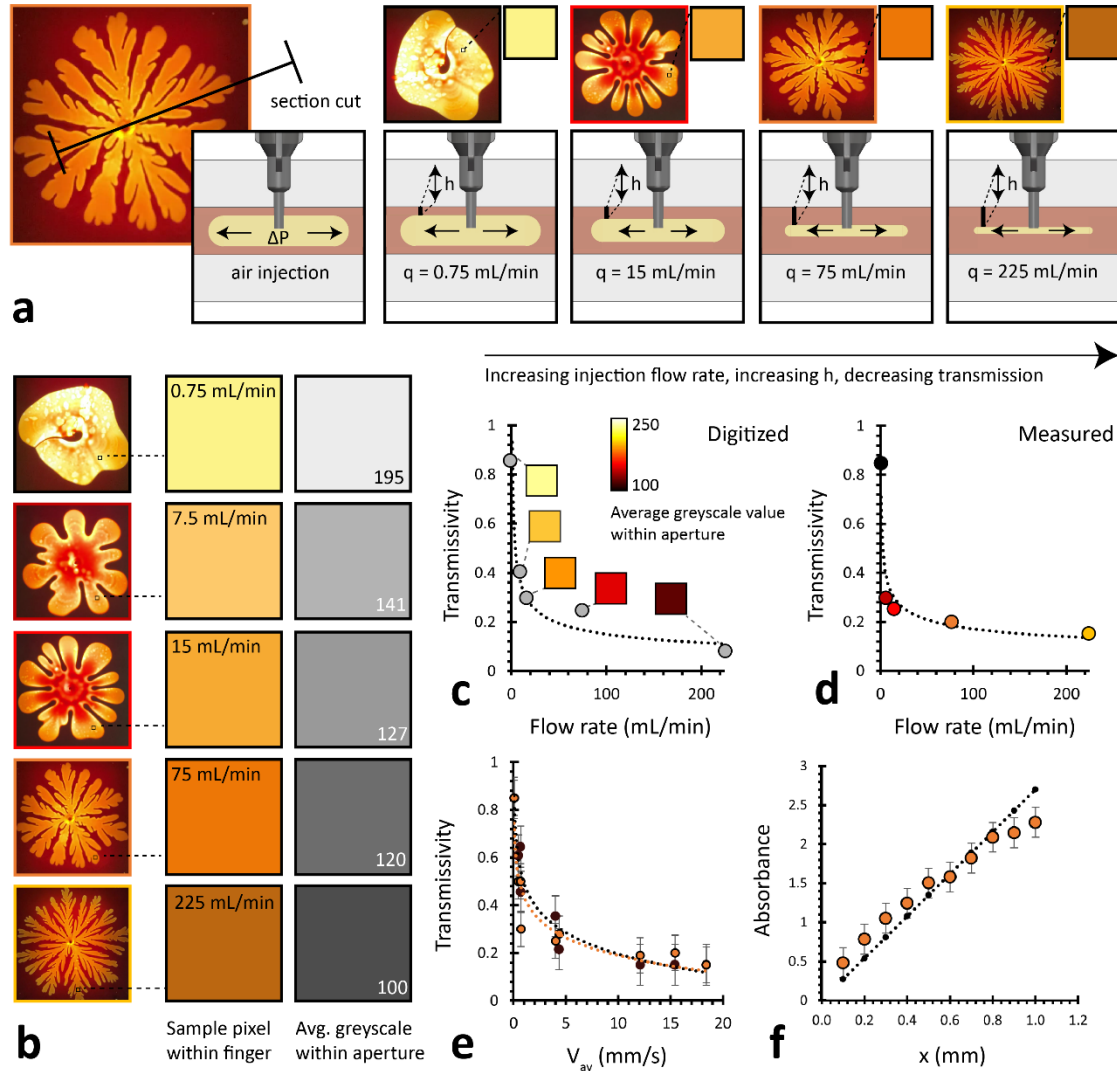


Figure 3. Aperture wetting and transmissivity can be programmed with nominal flow rate. (a) Top-down view of apertures generated at increasing injection flow rates, with corresponding section-cuts to demonstrate impact of injection velocity on thin film thickness within HS cell. Experimental pixel values also demonstrate changing optical transmissivity. (b) Pixel sampling from finger region of each aperture, indicative of differences in light transmissivity with consistent backlighting source (400 lux). Average greyscale value (between 0-255) measured across entire aperture region, quantifying differences in transmissivity. (c) Extrapolated transmissivity from digitized images and grey scale values from (c), remapped between measured light transmission values. (d) Measured transmissivity of apertures at different flow rates, showing good agreement with method from (c). Both (c-d) represent two different methods of validating wetting trend, suggesting variation in average film thickness within cell during aperture growth. (e) Transmissivity through aperture for different measured aperture front velocities, where velocity changes thin film thickness (h) and total optical path length through cell ($2h$). Velocity values were measured from video frames over local ($\sim 1 \text{ mm}^2$) areas. Black dots represent transmissivity data extrapolated from grey-scale video frames. Orange dots represent directly measured transmissivity data. (f) Orange dots represent measured absorbance of molasses as function of optical path length (x), where absorbance, $A = -\log_{10} T$. Black dots represent absorbance values generated using Beer-Lambert model. Best fit of dotted black line provides absorption coefficient, $\epsilon = 2700 \text{ m}^{-1}$ for molasses.

Phase space of optical programmability

Fig. 4a and Fig. 4b summarize the two flow-rate-dependent mechanisms for modulating cell light transmission introduced in Fig. 2-3, respectively. Injection flow rate impacts both the shape and opacity of an expanding aperture, while injection velocity impacts the size of an expanding aperture. Fig. 4c shows light transmission over time through a 30x30x1.3 cm³ HS cell. Apertures generated at higher flow rates develop and collapse much more rapidly, but are bound by lower maximum light transmission values. Fig. 4d shows a phase space for light transmission through the cell, demonstrating how flow rate impacts aperture area fraction and morphology (location along plot), as well as light transmission (colour of aperture), impacted by aperture opacity. Ultimately, a complete operational phase space for light transmission through the cell is shown in Fig. 4e. The first digital control – injection volume – is plotted along the y-axis, while the second digital control – injection flow rate – is plotted along the x-axis. The transmission gradient visualized along the plot was extrapolated from several dozen experimental data points, and represents a predictive model for our system’s transmissivity. Crucially, it demonstrates how two simple digital controls – injection volume (or time) and flow rate – can be modulated to achieve a given cell transmission.

Two flow-rate-dependent mechanisms for modulating light transmission

(1) Flow rate changes aperture morphology (2) Flow rate changes aperture wetting

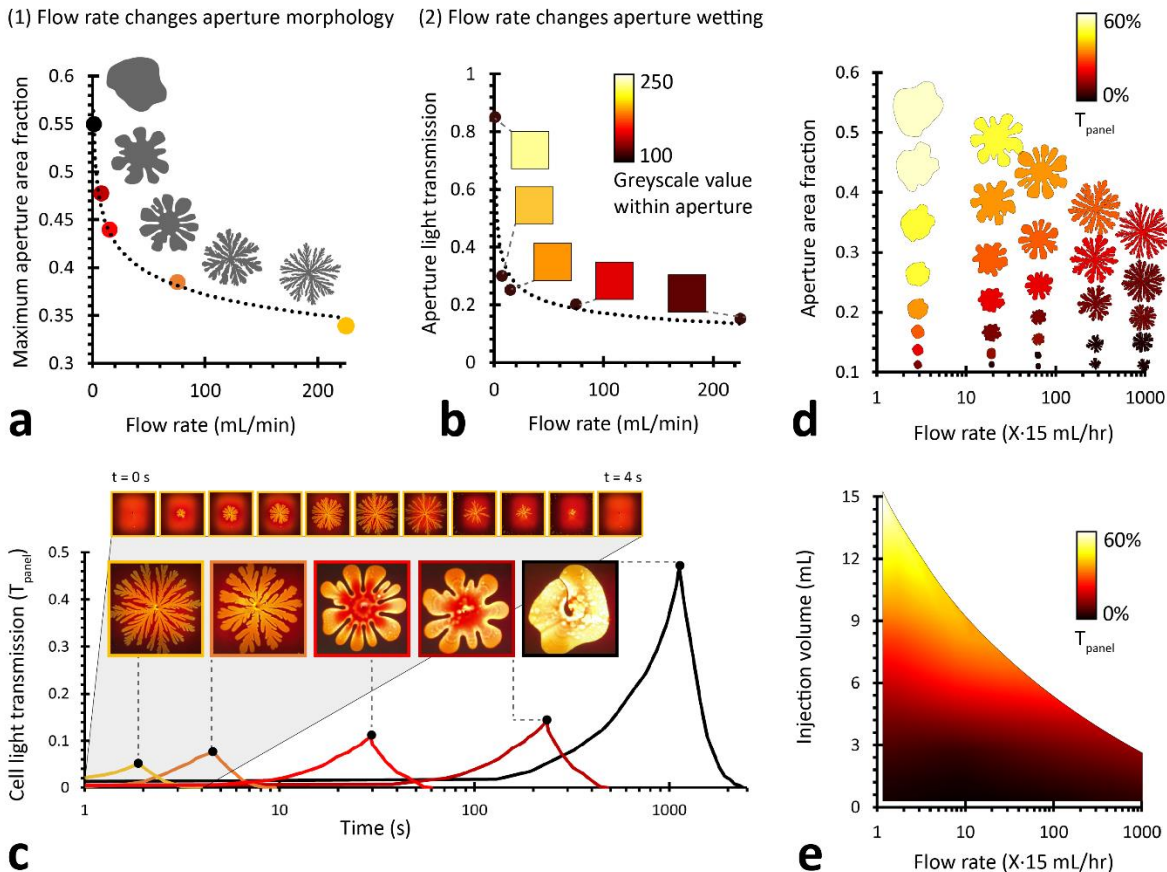


Figure 4. Operational phase space for transmissivity programmability. (a-b) Two mechanisms for modulating light transmission through a cell, each of which dependent on flow rate. (a) Aperture morphology and aperture area fraction can be programmed with flow rate. (b) Aperture wetting and light transmission intensity (area normalized) can be programmed with flow rate. Light transmission here is the measured light transmission through the aperture divided by the area of the aperture. This effect is confirmed by measuring average greyscale values within

the aperture area, when backlit and photographed. Colour corresponds to average greyscale value, where higher values correspond to greater light transmission from the back light through the aperture. (c) Measured light transmission through the cell over time for five different aperture expansion and retraction sequences at five different flow rates (0.75-225 mL/min). (d) Functional range of aperture: Measured light transmission through the cell as a function of both aperture size (represented as a fraction of the cell) and flow rate. (e) Digital control space over aperture: Measured light transmission through the cell as a function of both air injection volume and air injection flow rate. Flow rate values in (d-e) are in units of 15 mL/hr.

Recursive mathematical model to describe opacity

By adapting the relationships described in equations (3-4), we developed a recursive mathematical model to predict aperture transmissivity over time as a function of injection flow rate. The Aussillous and Quéré⁴⁷ relation – shown in equation (3), and called Taylor’s Law with $\varphi = 1.34$ and $\omega = 2.5$, describes how film thickness $h/0.5b$ increases as a function of Ca (Fig. 5a) within a capillary tube. We found that a modified version of the Taylor curve, with $\varphi = 2.0$ and $\omega = 3.2$, accurately described our empirical data within our HS cell (Fig. 5b), importantly providing a quantifiable link between local aperture velocity and thin film thickness, via a reverse calculation using equation (4) from measured transmissivity (Fig. 5b).

We simulated the calculation of velocity v_i , capillary number Ca_i , molasses film thickness h_i , absorbance A_i , and transmissivity T_i for successive radial ‘rings’ with radius R_i , up to a maximum radius R_n , throughout an aperture injection at constant flow rate q . This stepwise approach allowed us to dependently ‘construct’ the transmission (and relevant upstream properties) of the aperture at each timestamped radial ‘ring’ throughout its growth.

First, we described the radius R_i of our expanding aperture, increasing as a function of flow rate q , time t_i , and the depth of a cell within which it expands $b - 2h$ (equation (5)). Then, from empirical data (still frames), we extrapolated a relationship between maximum fingertip velocity V_{max} and q over an entire injection sequence, described in equation (6). This relation lets us find the duration of a complete injection for a given flow rate (equations (7-9)), allowing us to appropriately cut off our simulation once the aperture radius R_i reaches the maximum radius within our cell R_n (equation (10)).

We calculated velocity v_{i+1} at each timestep, as a function of R_{i+1} , R_i , q , and b (equation (11)). We then calculated capillary number Ca_i at each timestep, as a function of v_i . Next, using our modified version of Taylor’s Law, we calculated h_i , as a function of Ca_i (equation (13)). And finally, using the Beer-Lambert Law, we calculated A_i , and eventually T_i , as a function of Ca_i (equations (14-15)).

A small amount of ‘sacrificial recursion’ was required, because R_i fundamentally depends on h_i , while h_i fundamentally depends on R_i . To deal with this condition, we first simulated R_0 and R_1 , assuming that $h_{0,1}$ were both negligible (zero). Using R_0 and R_1 , we were able to calculate V_1 , Ca_1 , and h_1 , which we then fed into the definition of R_2 – enabling the generation of h_2 , then R_3 , then h_3 , and so forth. Ultimately, we found that feeding h_i into the definition of R_i had a negligible impact on the transmission predictions of our model, and we therefore assumed h_i to be negligible in the calculation of V_i .

Once T_i - T_n were calculated for an entire injection sequence, we averaged their values over the relative area of each radial ring to find the average transmissivity across the entire aperture T_{avg} (equation (16)). We simulated this sequence for a continuous list of flow rates between 0.75-225 mL/min, to find $t_n(q)$ (Fig. 5c), $V_{avg}(q)$ (Fig. 5d), $Ca_{avg}(q)$ (Fig. 5e), $A_{avg}(q)$ (Fig. 5f), and, ultimately, $T_{avg}(q)$ (Fig. 5g), which we compared, and found good similarity, to our experimental values (Fig. 5g).

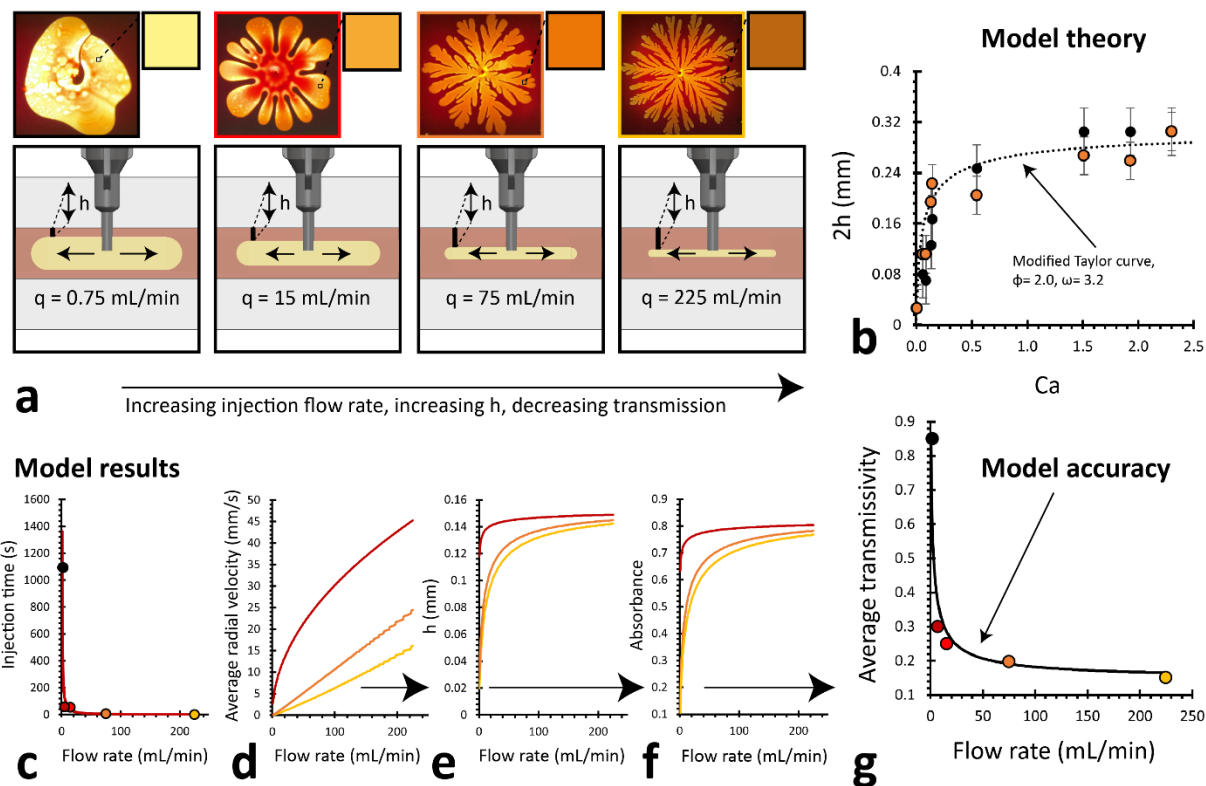


Figure 5. Mathematical model for measuring aperture transparency as function of flow rate. (a) Top-down view of apertures generated at increasing injection flow rates, with corresponding section-cuts to demonstrate impact of injection velocity on thin film thickness within HS cell. (b) Calculated thin film thickness versus Ca (Ca is directly proportional to velocity). Thickness values calculated using Beer-Lambert model with $\epsilon = 2700 \text{ m}^{-1}$, from Fig. 3f.

Dotted black line represents fitted curve using a modified version of the Taylor model⁴⁷ for the thickness of a wetting film as a function of Ca . Fitting parameters of $\phi = 2.0$ and $\omega = 3.2$ were used. (c) Modelled total injection time for aperture as a function of flow rate. Coloured dots represent true times from experiment. (d) Modelled average radial velocity as a function of flow rate. Burgundy, orange, and yellow curves represent maximum, mean, and minimum values calculated at each modelled flow rate. (e) Modelled thin film thickness as a function of flow rate. Burgundy, orange, and yellow curves represent maximum, mean, and minimum values calculated at each modelled flow rate. (f) Modelled absorbance as a function of flow rate. Burgundy, orange, and yellow curves represent maximum, mean, and minimum values calculated at each modelled flow rate. (g) Modelled transmissivity as a function of flow rate. Displayed curve represent mean value calculated at each modelled flow rate. Model shows good accuracy for predicting average transmissivity, when compared to measured values.

Multiplexed dynamic digital control

Our system's pneumatic mechanics and digital controls lend themselves to large-area scalability. We accordingly fabricated a multiplexed (4x4) HS cell, with a modified system design. To deal with the change in contained fluid volume during injection, we replaced one of the rigid HS cell walls with a 0.1-mm-thick sheet of PMMA. This approach allowed us to omit bladder hosing, and we fabricated each HS cell 'pixel' with only one outlet port – which we kept open to maintain atmospheric pressure during preliminary molasses filling (Fig. 6a).

Each of the sixteen inlet hoses was connected to a digitally-controlled peristaltic pump (electronic setup pictured in Extended Data Fig. 3). We developed a series of dynamically-patterned 'movies' by

coordinated the digital actuation of pneumatic injections and retractions within our multiplexed HS cell over time (Fig. 6b). While the dynamics and optical behaviours are distinct in this elastic device from those shown and modelled for the rigid HS device in Fig. 1-5, the digital capabilities demonstrated in Fig. 6b and ED Movie 1 can be applied to direct spatiotemporal patterning across a variety of pneumatically-accessible, multiplexed fluid systems.

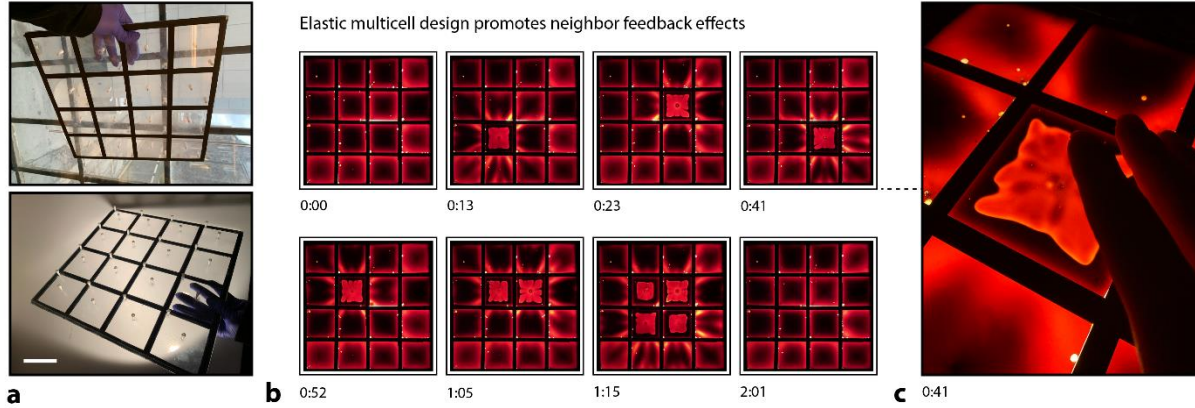


Figure 6. Digital control over dynamic multiport pneumatic injections. (a) Images of empty sixteen-cell device prior to fluid injection. Scale bar is 10 cm. (b) Still frame captures from Movie S1, showing digitally-actuated spatiotemporal control of air injections and pattern dynamics. (c) Still frame capture from sequence demonstrated in Movie S1 showing single air injection within panel. Hand pictured to illustrate scale.

Model Calculation Section

Consider an expanding ‘two-dimensional’ air bubble with a radius R_i that increases as a function of flow rate q , time t_i , and the depth of a cell it expands within $b - 2h$,

$$(5) \quad R_i = \sqrt{\frac{qt_i}{\pi(b-2h)}}$$

We extrapolated from our physical experiments the maximum velocity of the air bubble V_{max} as a function of the flow rate of the air injection q ,

$$(6) \quad V_{max} = \frac{R_{cell}}{0.0000003 \cdot q^{(-1.222)}}$$

The elapsed time of a complete injection can therefore be written as,

$$(7) \quad t_n = \frac{R_{cell}}{V_{max}}$$

The total time of the air injection t_n is a function of the square-shaped radius of the container within which it grows R_{cell} and the velocity of the air bubble V_{max} (how quickly it reaches the edge of its container). For the entire growth period,

$$(8) \quad t_i < \frac{R_{cell}}{V_{max}}$$

But once the following expression becomes true, then t_n has been reached,

$$(9) \quad t_i = \frac{R_{cell}}{V_{max}}$$

The maximum radius of the air bubble R_n depends on the total time of the air injection t_n , and determines when the model needs to be turned off,

$$(10) \quad R_n = \sqrt{\frac{qt_n}{\pi(b-2h)}}$$

The average velocity v_{i+1} between time t_i and time t_{i+1} , is given by,

$$(11) \quad v_{i+1} = \frac{q}{\pi b} \cdot \frac{R_{i+1} - R_i}{R_{i+1}^2 - R_i^2}$$

The capillary number Ca_i is a function of the average velocity v_i ,

$$(12) \quad Ca_i = \frac{v_i \Delta n}{\sigma}$$

The thickness of the leftover fluid h_i (not displaced by a moving air bubble) is a function of the capillary number Ca_i , and is given by Aussillous and Qu  r  ⁴⁷, modified from Bretherton⁴⁶, as,

$$(13) \quad h_i = \frac{0.5b \cdot \varphi \cdot Ca_i^{2/3}}{1 + ([\varphi \cdot \omega] \cdot Ca_i^{2/3})}$$

Absorbance A_i , according to the Beer-Lambert law⁴⁸, is related to the thickness of the fluid film h_i through which light must travel,

$$(14) \quad A_i = 2h_i \cdot \varepsilon$$

Transmittance T_i is related to absorbance A_i ,

$$(15) \quad T_i = 10^{[-1 \cdot A_i]}$$

The average transmittance across the fluid bubble $T_{avg}(q)$ is the average transmittance at every time stamp of the air bubble injection,

$$(16) \quad T_{avg}(q) = \frac{1}{n} \sum_{i=1}^n T_i$$

Acknowledgements

We are indebted to Stephen Morris and Howard Stone for their helpful insights. We also acknowledge Nicholas Hoban for his guidance on proceeding research.

Author contributions

Conceptualization: RK, CK, BDH

Methodology: RK, CK, BDH

Physical experimentation: RK

Mathematical model design and implementation: RK, CK, EH

Visualization: RK

Electronic system design: KN

Funding acquisition: BDH

Writing: RK

Editing and revision: RK, CK, KN, JAJ, BDH

Data availability

All data and model code can be provided by the corresponding author upon reasonable request.

Competing interests

The authors declare no competing interests.

References

- 1 Pérez-Lombard, L., Ortiz, J. & Pout, C. A review on buildings energy consumption information. *Energy and Buildings* **40**, 394-398, doi:<https://doi.org/10.1016/j.enbuild.2007.03.007> (2008).
- 2 U.S.D.o.E. Annual Energy Outlook 2021 (AEO2021). (2021).
- 3 Zeidler, C., Schubert, D. & Vrakking, V.
- 4 Gutierrez, M. P. & Lee, L. P. Multiscale Design and Integration of Sustainable Building Functions. *Science* **341**, 247-248 (2013).
- 5 Loonen, R. C. G. M., Trčka, M., Cóstola, D. & Hensen, J. L. M. Climate adaptive building shells: State-of-the-art and future challenges. *Renewable and Sustainable Energy Reviews* **25**, 483-493, doi:<https://doi.org/10.1016/j.rser.2013.04.016> (2013).
- 6 Kay, R., Nitiema, K., Katrycz, C., Jakubiec, A. & Hatton, B. D. Self-organizing fluids for active building facades (accepted). *Nature Communications* (2022).
- 7 Khandelwal, H., Schenning, A. P. H. J. & Debije, M. G. Infrared Regulating Smart Window Based on Organic Materials. *Advanced Energy Materials* **7**, 1602209, doi:10.1002/aenm.201602209 (2017).
- 8 Hatton, B., Mishchenko, L., Davis, S., Sandhage, K. H. & Aizenberg, J. Assembly of large-area, highly ordered, crack-free inverse opal films. *Proceedings of the National Academy of Sciences* **107**, 10354, doi:10.1073/pnas.1000954107 (2010).
- 9 Rossiter, J., Yap, B. & Conn, A. Biomimetic chromatophores for camouflage and soft active surfaces. *Bioinspir Biomim* **7**, 036009, doi:10.1088/1748-3182/7/3/036009 (2012).
- 10 Xu, C., Stiubianu, G. T. & Gorodetsky, A. A. Adaptive infrared-reflecting systems inspired by cephalopods. *Science* **359**, 1495, doi:10.1126/science.aar5191 (2018).
- 11 Cupelli, D. *et al.* Self-adjusting smart windows based on polymer-dispersed liquid crystals. *Solar Energy Materials and Solar Cells* **93**, 2008-2012, doi:<https://doi.org/10.1016/j.solmat.2009.08.002> (2009).
- 12 Drzaic, P. S. Polymer dispersed nematic liquid crystal for large area displays and light valves. *Journal of Applied Physics* **60**, 2142-2148, doi:10.1063/1.337167 (1986).
- 13 Van Konynenburg, P., Marsland, S. & McCoy, J. Solar radiation control using NCAP liquid crystal technology. *Solar Energy Materials* **19**, 27-41, doi:[https://doi.org/10.1016/0165-1633\(89\)90021-X](https://doi.org/10.1016/0165-1633(89)90021-X) (1989).
- 14 Vergaz, R., Pena, J., Barrios, D., Pérez, I. & Torres, J. Electrooptical behaviour and control of a suspended particle device. *Opto-Electronics Review* **15**, 154-158, doi:<https://doi.org/10.2478/s11772-007-0013-9> (2007).
- 15 Vergaz, R., Sánchez-Pena, J.-M., Barrios, D., Vázquez, C. & Contreras-Lallana, P. Modelling and electro-optical testing of suspended particle devices. *Solar Energy Materials and Solar Cells* **92**, 1483-1487, doi:<https://doi.org/10.1016/j.solmat.2008.06.018> (2008).
- 16 Lampert, C. M. Chromogenic smart materials. *Materials Today* **7**, 28-35, doi:[https://doi.org/10.1016/S1369-7021\(04\)00123-3](https://doi.org/10.1016/S1369-7021(04)00123-3) (2004).
- 17 Niklasson, G. A. & Granqvist, C. G. Electrochromics for smart windows: thin films of tungsten oxide and nickel oxide, and devices based on these. *Journal of Materials Chemistry* **17**, 127-156, doi:10.1039/B612174H (2007).
- 18 Fernández, J. E. Materials for Aesthetic, Energy-Efficient, and Self-Diagnostic Buildings. *Science* **315**, 1807, doi:10.1126/science.1137542 (2007).
- 19 Lee, E. S. & DiBartolomeo, D. L. Application issues for large-area electrochromic windows in commercial buildings. *Solar Energy Materials and Solar Cells* **71**, 465-491, doi:[https://doi.org/10.1016/S0927-0248\(01\)00101-5](https://doi.org/10.1016/S0927-0248(01)00101-5) (2002).
- 20 Lampert, C. Large-Area Smart Glass And Integrated Photovoltaics. *Solar Energy Materials and Solar Cells* **76**, 489-499, doi:10.1016/S0927-0248(02)00259-3 (2003).

- 21 Gillaspie, D. T., Tenent, R. C. & Dillon, A. C. Metal-oxide films for electrochromic applications: present technology and future directions. *Journal of Materials Chemistry* **20**, 9585-9592, doi:10.1039/COJM00604A (2010).
- 22 Granqvist, C. G. Electrochromics for smart windows: Oxide-based thin films and devices. *Thin Solid Films* **564**, 1-38, doi:<https://doi.org/10.1016/j.tsf.2014.02.002> (2014).
- 23 Wang, Y., Runnerstrom, E. L. & Milliron, D. J. Switchable Materials for Smart Windows. *Annu Rev Chem Biomol Eng* **7**, 283-304, doi:10.1146/annurev-chembioeng-080615-034647 (2016).
- 24 Li, X.-H., Liu, C., Feng, S.-P. & Fang, N. X. Broadband Light Management with Thermochromic Hydrogel Microparticles for Smart Windows. *Joule* **3**, 290-302, doi:<https://doi.org/10.1016/j.joule.2018.10.019> (2019).
- 25 Granqvist, C. G., Lansåker, P. C., Mlyuka, N. R., Niklasson, G. A. & Avendaño, E. Progress in chromogenics: New results for electrochromic and thermochromic materials and devices. *Solar Energy Materials and Solar Cells* **93**, 2032-2039, doi:<https://doi.org/10.1016/j.solmat.2009.02.026> (2009).
- 26 Granqvist, C. G. Transparent conductors as solar energy materials: A panoramic review. *Solar Energy Materials and Solar Cells* **91**, 1529-1598, doi:<https://doi.org/10.1016/j.solmat.2007.04.031> (2007).
- 27 Granqvist, C. G. Chromogenic materials for transmittance control of large-area windows. *Critical Reviews in Solid State and Materials Sciences* **16**, 291-308, doi:10.1080/10408439008242184 (1990).
- 28 Yu, C. *et al.* Adaptive optoelectronic camouflage systems with designs inspired by cephalopod skins. *Proc Natl Acad Sci U S A* **111**, 12998-13003, doi:10.1073/pnas.1410494111 (2014).
- 29 Fazel, A., Izadi, A. & Azizi, M. Low-cost solar thermal based adaptive window: combination of energy-saving and self-adjustment in buildings. *Solar Energy* **133**, 274-282 (2016).
- 30 Wood, D. M., Correa, D., Krieg, O. D. & Menges, A. Material computation—4D timber construction: Towards building-scale hygroscopic actuated, self-constructing timber surfaces. *International Journal of Architectural Computing* **14**, 49-62, doi:10.1177/1478077115625522 (2016).
- 31 Reichert, S., Menges, A. & Correa, D. Meteorosensitive architecture: Biomimetic building skins based on materially embedded and hygroscopically enabled responsiveness. *Computer-Aided Design* **60**, 50-69, doi:<https://doi.org/10.1016/j.cad.2014.02.010> (2015).
- 32 Poppinga, S. *et al.* Toward a New Generation of Smart Biomimetic Actuators for Architecture. *Advanced Materials* **30**, 1703653, doi:<https://doi.org/10.1002/adma.201703653> (2018).
- 33 Drozdowski, Z. & Gupta, S. in *Proceedings of the 29th Annual Conference of the Association for Computer Aided Design in Architecture*. 105-109.
- 34 Lienhard, J. *et al.* Flectofin: a hingeless flapping mechanism inspired by nature. *Bioinspiration & Biomimetics* **6**, 045001, doi:10.1088/1748-3182/6/4/045001 (2011).
- 35 Park, D. *et al.* Dynamic daylight control system implementing thin cast arrays of polydimethylsiloxane-based millimeter-scale transparent louvers. *Building and Environment* **82**, 87-96, doi:<https://doi.org/10.1016/j.buildenv.2014.07.016> (2014).
- 36 Viereck, V. *et al.* in *2008 5th International Conference on Networked Sensing Systems*. 135-139.
- 37 Nouvel, J. & Fessy, G. *Institut du Monde arabe*. (Archivision, 1995).
- 38 Hatton, B. D. *et al.* An artificial vasculature for adaptive thermal control of windows. *Solar Energy Materials and Solar Cells* **117**, 429-436, doi:<https://doi.org/10.1016/j.solmat.2013.06.027> (2013).
- 39 Kay, R., Jakubiec, J. A., Katrycz, C. & Hatton, B. D. *Multilayered optofluidics for active building facades (unpublished)* (2022).

- 40 Kay, R., Katrycz, C., Heimlich, E. & Hatton, B. D. Programmable droplets: Leveraging digitally-responsive flow fields to actively tune liquid morphologies (accepted). *PLOS One* (2022).
- 41 Kay, R. *et al.* Shape-programmable fluid bubbles for responsive building skins. *Journal of Building Engineering* **48**, 103942, doi:<https://doi.org/10.1016/j.jobbe.2021.103942> (2022).
- 42 Kay, R., Katrycz, C. & Hatton, B. D. The potential for thermoresponsive fluid self-organization within dynamic building facades (under review). *Journal of Building Physics* (2022).
- 43 Bischofberger, I., Ramachandran, R. & Nagel, S. R. Fingering versus stability in the limit of zero interfacial tension. *Nature Communications* **5**, 5265, doi:10.1038/ncomms6265 (2014).
- 44 Bischofberger, I. & Nagel, S. R. Fluid instabilities that mimic animal growth. *Physics Today* **69**, 70-71 (2016).
- 45 Saffman, P. G. & Taylor, G. I. The penetration of a fluid into a porous medium or Hele-Shaw cell containing a more viscous liquid. *Proceedings of the Royal Society of London. Series A. Mathematical and Physical Sciences* **245**, 312-329, doi:10.1098/rspa.1958.0085 (1958).
- 46 Bretherton, F. P. The motion of long bubbles in tubes. *Journal of Fluid Mechanics* **10**, 166-188, doi:10.1017/S0022112061000160 (1961).
- 47 Aussillous, P. & Quéré, D. Quick deposition of a fluid on the wall of a tube. *Physics of Fluids* **12**, 2367-2371, doi:10.1063/1.1289396 (2000).
- 48 Swinehart, D. F. The beer-lambert law. *Journal of chemical education* **39**, 333 (1962).